*machines*

MDPI

*Article*

# Singular Value-Based Analysis of Current Decoupling Control Effect of Permanent Magnet Synchronous Motors

**Tianyi Zhang, Qi Li *, Pengbin Xu, Dafang Wang, Haoyu Zhou and Jinhuan Zhao**

School of Automotive Engineering, Harbin Institute of Technology, Weihai 264209, China; 2023212557@stu.hit.edu.cn (T.Z.); 24b308025@stu.hit.edu.cn (P.X.); 13863009863@163.com (D.W.); 24s130323@stu.hit.edu.cn (H.Z.); 25s130233@stu.hit.edu.cn (J.Z.)

* Correspondence: liqihit2019@hit.edu.cn

**Abstract**

The dq-axis coupling effect significantly influences the vector control performance of permanent magnet synchronous motors (PMSMs), and traditional proportional-integral (PI) control cannot control the system as desired. Extensive studies have addressed this coupling effect. However, traditional evaluation methods based on pole–zero distribution are not intuitive, which is unfavorable for engineers to select and apply decoupling strategies. This paper employed singular value analysis to assess coupling trends and magnitude–frequency characteristics of the system. In consideration of the effects of rotor speed, parameter estimation error, and digital delay, a comprehensive evaluation of controllers was conducted. This evaluation included feedforward, feedback, and internal model control (IMC) decoupling, with the analysis facilitated by singular value plots. Under the parameters chosen in this paper, the feedforward decoupling controller improves slightly in decoupling under time delay, but higher rotor speed degrades its performance more. The feedback decoupling controller worsens as the system's overshoot rate surges from 19.4% to 33.4% under the effect of time delay, though it can decouple completely under ideal conditions. It is evident that the efficacy of all strategies is diminished in the presence of parameter estimation deviation. In contrast, the internal model decoupling controller shows better decoupling capability and stronger robustness, while its overshoot remains under 24%. The effectiveness of the proposed method was confirmed through a combination of simulations and experiments.

**Keywords:** current loop decoupling; permanent magnet synchronous motors (PMSMs); singular values

Check for updates

Academic Editors: Karol Wróbel and Piotr Derugo

Received: 10 August 2026
Revised: 31 August 2026
Accepted: 4 September 2026
Published: 7 September 2026

**Copyright:** © 2026 by the authors. Licensee MDPI, Basel, Switzerland. This article is an open access article distributed under the terms and conditions of the Creative Commons Attribution (CC BY) license.

## 1. Introduction

Permanent magnet synchronous motors (PMSMs) have been widely applied in the electric drive systems of electric vehicles due to their high power density, high efficiency, and structural compactness [1–6]. Field-oriented control (FOC) is an important method to accurately control PMSMs. Through Clarke and Park transformations, the PMSM voltage equations are converted from the three-phase coordinate system into the dq-axis synchronous rotating two-phase coordinate system. Proportional-integral (PI) control is then used to dynamically regulate the current loop [7,8].

However, due to the presence of speed-dependent coupling terms, any dynamics in one axis inevitably introduces disturbance in the other axis, and the coupling becomes stronger under high-speed conditions [9,10]. This results in discrepancies between the

reference and actual current values and affects the current's dynamic trajectory, which will then influence the whole control of the motor [11,12]. In that case, conventional PI control cannot achieve the desired performance and may even lead to instability. Therefore, decoupling methods are required to regulate dq-axis currents independently and improve the transient behavior [13].

Early work [14] applied feedback decoupling to PMSMs, and feedforward decoupling was later adopted in [15]. Both strategies provide better regulation compared with conventional PI control. Yet, they are mainly model-based and thus sensitive to parameter variations. Under large parameter errors, their dynamic decoupling performance is poor [16]. To address this limitation, [17] proposed internal model control (IMC) decoupling control for PMSMs based on the internal model principle. A similar deviation decoupling method was proposed in [18] and further extended to PMSM drive systems in [19]. The two strategies demonstrate better control performance and robustness and are widely adopted in practice. More recently, research has gradually shifted from focusing on mathematical models to developing advanced control methods, integrating big data, real-time computation, and intelligent algorithms [20].

Extensive studies on decoupling strategies have been conducted. However, relatively few works have addressed intuitive evaluation methods for decoupling effectiveness. Most evaluations rely on simulations and experiments. But it is cumbersome to compare the performance under different operating conditions. To address this issue, the paper [21] adopts pole–zero distribution and Bode plots to analyze several decoupling strategies with complex vector representation, which transforms dq-axis vectors from a multi-input multi-output (MIMO) system into a single-input single-output (SISO) form [22]. However, the focus of this method lies in analyzing stability and dynamic performance. There is no intuitive and unified metric for coupling level. In [23], the dynamic relative gain array (DRGA) is introduced. Based on the transfer function matrix, the study compares four decoupling controllers through coupling content intuitively represented by the RGA number. Nevertheless, this approach attends to the representation of coupling content but lacks the manifestation of system dynamic response characteristics, which is the direct effect of coupling.

To evaluate both the system coupling trend and frequency-domain characteristics, this paper introduces singular value analysis based on a MIMO framework. The proposed analysis is based on a linearized current-loop model of a permanent magnet synchronous motor centered on a specific operating point. Given the widespread application of electric motors in the automotive industry, the parameter selection and operating conditions discussed in this paper are primarily derived from automotive drive motor scenarios. First, the overall state-space equations of the controllers and the motor drive systems are derived. Then, frequency-domain singular value analysis is conducted to investigate the effects of motor speed, parameter estimation errors, and digital delay on the controller's performance. Finally, simulations and experiments are carried out to verify the effectiveness of the proposed method.

## 2. Description of the Frequency-Domain Singular Value Analysis Method

The singular value analysis method is part of linear system theory and is applied in the evaluation of MIMO systems. It reflects the coupling among variables and the magnitude–frequency characteristics of the system. For a MIMO system, the transfer function matrix G(s) can be derived from the state-space equations, and singular value decomposition (SVD) can be performed on G(s).

The maximum and minimum singular values are denoted as follows:

$$\sigma_{\max}(\mathbf{G}) = \max_{x \neq 0} \frac{||\mathbf{Gx}||_2}{||\mathbf{x}||_2} \tag{1}$$

$$\sigma_{\min}(\mathbf{G}) = \min_{x \neq 0} \frac{||\mathbf{Gx}||_2}{||\mathbf{x}||_2} \tag{2}$$

The system gain lies between the maximum and minimum singular values and varies with frequency.

The condition number of G(s) quantifies the coupling condition by taking the ratio of the maximum and minimum singular values [24], which can be expressed as follows:

$$\kappa(\mathbf{G}) = \frac{\sigma_{\max}(\mathbf{G})}{\sigma_{\min}(\mathbf{G})} \tag{3}$$

A value closer to one indicates that the output gain is less strongly dependent on the input direction, while a larger value implies stronger dependence. In PMSM control systems employing parameter tuning based on zero–pole cancellation, the gains depend on the bandwidths, which are identical in a synchronous rotating two-phase coordinate system. In the singular value plot, the coupling content can be intuitively observed from the distance between the maximum and minimum singular value curves.

## 3. State-Space Model of Permanent Magnet Synchronous Motor

After the coordinate transformation, the voltage–current equations of the PMSM can be represented in the synchronous rotating reference frame. In scalar form:

$$\begin{cases} u_{sd} = R_s i_{sd} + L_d \frac{di_{sd}}{dt} - \omega_e L_q i_{sq} \\ u_{sq} = R_s i_{sq} + L_q \frac{di_{sq}}{dt} + \omega_e L_d i_{sd} + \omega_e \psi_f \end{cases} \tag{4}$$

where $u_{sd}$ and $u_{sq}$ are stator voltages in the d-axis and q-axis, $i_{sd}$ and $i_{sq}$ are stator currents in the d-axis and q-axis, $L_d$ and $L_q$ are stator inductances in the d-axis and q-axis, $\omega_e$ is the electrical angular velocity, $R_s$ is the stator resistance, and $\psi_f$ is rotor flux linkage. Values are listed in Table 1.

**Table 1.** Variables in the equation.

| Variable | Symbol |
|---|---|
| stator voltages in the d-axis | $u_{sd}$ |
| stator voltages in the q-axis | $u_{sq}$ |
| stator currents in the d-axis | $i_{sd}$ |
| stator currents in the q-axis | $i_{sq}$ |
| stator inductances in the d-axis | $L_d$ |
| stator inductances in the q-axis | $L_q$ |
| electrical angular velocity | $\omega_e$ |
| stator resistance | $R_s$ |
| rotor flux linkage | $\psi_f$ |
| integral coefficient | $K_i$ |
| d-axis proportional coefficient | $K_{pd}$ |
| q-axis proportional coefficient | $K_{pq}$ |
| control bandwidth | $BW$ |

From the above equations, it can be observed that the dq-axes contain the coupling terms $\omega_e L_q i_{sq}$ and $\omega_e L_d i_{sd}$. Conventional SISO models usually neglect these coupling terms. However, under high-speed operating conditions, their magnitudes increase, so the

influence on system control performance cannot be ignored. To characterize the coupling behavior of the system facilitating singular value analysis, we employ the state-space representation to model the motor as a MIMO system.

In practical applications such as electric vehicles, $\omega_e$ cannot change abruptly due to inertia. More importantly, it changes much more slowly than the stator current [25]. Therefore, the permanent magnet back electromotive force associated with it can be regarded as a quasi-static disturbance within a control cycle. It is further assumed that this disturbance is completely compensated. By defining the system input as $\mathbf{U}_s = [u_{\mathrm{sd}}\ u_{\mathrm{sq}}]^T$ and the output as $\mathbf{I}_s = [i_{\mathrm{sd}}\ i_{\mathrm{sq}}]^T$ [26], the state-space model of the motor can be formulated as follows:

$$\begin{cases} \dot{\mathbf{I}}_s = \mathbf{A}_m \mathbf{I}_s + \mathbf{B}_m \mathbf{U}_s \\ \mathbf{I}_s = \mathbf{C}_m \mathbf{I}_s + \mathbf{D}_m \mathbf{U}_s \end{cases} \tag{5}$$

where $\mathbf{A}_m = \begin{bmatrix} -\frac{R_s}{L_d} & \frac{L_q \omega_e}{L_d} \\ -\frac{L_d \omega_e}{L_q} & -\frac{R_s}{L_q} \end{bmatrix}$, $\mathbf{B}_m = \begin{bmatrix} \frac{1}{L_d} & 0 \\ 0 & \frac{1}{L_q} \end{bmatrix}$, $\mathbf{C}_m = \begin{bmatrix} 1 & 0 \\ 0 & 1 \end{bmatrix}$, $\mathbf{D}_m = 0$.

## 4. State-Space Representation of the Current Decoupling Control System

In this section, decoupling controllers are incorporated to formulate the overall state-space model of the PMSM control system for subsequent analysis.

### *4.1. Feedforward Decoupling*

Feedforward decoupling uses the reference currents to compensate for the coupling term in open loop and is sensitive to parameter error. The structure diagram is shown in Figure 1.

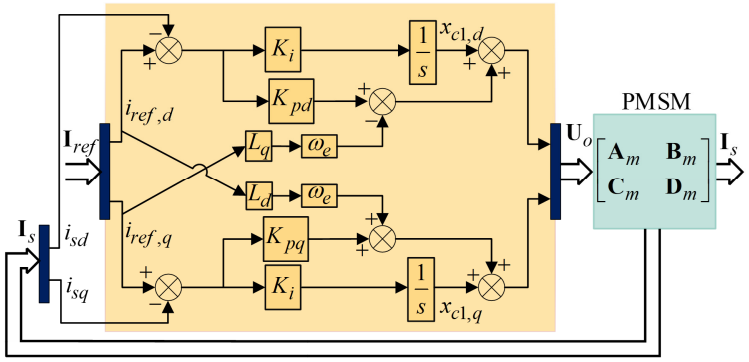



**Figure 1.** Structure diagram of feedforward decoupling.

Here, $K_i$ is the integral coefficient, $K_{pd}$ is the d-axis proportional coefficient, and $K_{pq}$ is the q-axis proportional coefficient. These values are related to motor parameters and control bandwidth:

$$\begin{cases} K_i = BW \times \hat{R}_s \\ K_{pd} = BW \times \hat{L}_d \\ K_{pq} = BW \times \hat{L}_q \end{cases} \tag{6}$$

where $BW$ is the control bandwidth, $\hat{R}_s$ is the estimated value of stator resistance, $\hat{L}_d$ is the estimated value of stator inductance on the d-axis, $\hat{L}_q$ is the estimated value of stator inductance on the q-axis.

When ignoring time delay, the output voltage of the controller is equal to the input voltage of the motor, that is

$$\mathbf{U}_o = \mathbf{U}_s \tag{7}$$

The system input can be defined as $\mathbf{I}_{ref} = [i_{ref,\mathrm{d}}\ i_{ref,\mathrm{q}}]^T$ and $\mathbf{I}_s = [i_{\mathrm{sd}}\ i_{\mathrm{sq}}]^T$, which are the reference currents and stator currents, respectively. While the controller state is defined as $\mathbf{x}_{c1} = [x_{\mathrm{c1,d}}\ x_{c1,q}]^T$, the state-space model of the feedforward controller can be expressed as follows:

$$\begin{cases} \dot{\mathbf{x}}_{c1} = \mathbf{A}_f\mathbf{x}_{c1} + \mathbf{B}_{f1}\mathbf{I}_s + \mathbf{B}_{f2}\mathbf{I}_{ref} \\ \mathbf{U}_o = \mathbf{C}_f\mathbf{x}_{c1} + \mathbf{D}_{f1}\mathbf{I}_s + \mathbf{D}_{f2}\mathbf{I}_{ref} \end{cases} \tag{8}$$

where $\mathbf{A}_f = 0$, $\mathbf{B}_{f1} = \begin{bmatrix} -K_i & 0 \\ 0 & -K_i \end{bmatrix}$, $\mathbf{B}_{f2} = \begin{bmatrix} K_i & 0 \\ 0 & K_i \end{bmatrix}$, $\mathbf{C}_f = \begin{bmatrix} 1 & 0 \\ 0 & 1 \end{bmatrix}$, $\mathbf{D}_{f1} = \begin{bmatrix} -K_{pd} & 0 \\ 0 & -K_{pq} \end{bmatrix}$, $\mathbf{D}_{f2} = \begin{bmatrix} K_{pd} & -L_q\omega_e \\ L_d\omega_e & K_{pq} \end{bmatrix}$.

By combining (5), (7), (8), the whole system of feedforward decoupling can be described as follows:

$$\begin{cases} \begin{bmatrix} \dot{\mathbf{x}}_{c1} \\ \dot{\mathbf{I}}_s \end{bmatrix} = \begin{bmatrix} \mathbf{A}_f & \mathbf{B}_{f1} \\ \mathbf{B}_m\mathbf{C}_f & \mathbf{A}_m + \mathbf{B}_m\mathbf{D}_{f1} \end{bmatrix} \begin{bmatrix} \mathbf{x}_{c1} \\ \mathbf{I}_s \end{bmatrix} + \begin{bmatrix} \mathbf{B}_{f2} \\ \mathbf{B}_m\mathbf{D}_{f2} \end{bmatrix} \mathbf{I}_{ref} \\ \mathbf{I}_s = \begin{bmatrix} 0 & \mathbf{I} \end{bmatrix} \begin{bmatrix} \mathbf{x}_{c1} \\ \mathbf{I}_s \end{bmatrix} \end{cases} \tag{9}$$

### *4.2. Feedback Decoupling*

The feedback decoupling method compensates for the coupling terms using the motor stator currents, which can be adjusted according to the current error. Theoretically, currents of the dq-axes can be fully decoupled. But in practice, the feedback currents are not equal to the actual currents due to the time-delay effect. Its effectiveness is also degraded by time delay, which will be analyzed in Section 5. Also, the feedback currents may bring some noise, like PWM Ripple. The structure diagram is shown in Figure 2.

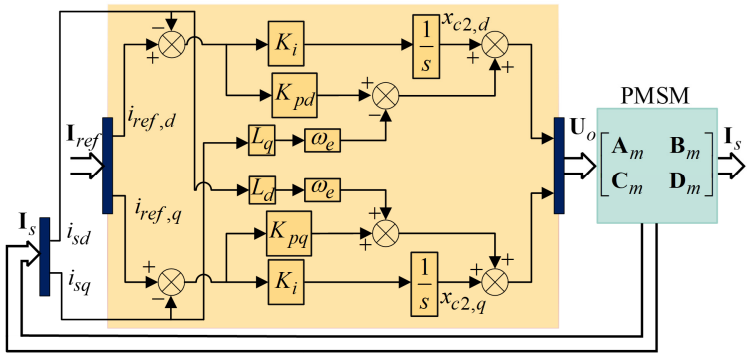



**Figure 2.** Structure diagram of feedback decoupling.

Similar to the step in (8), the state-space model of the feedback controller can be expressed as follows:

$$\begin{cases} \dot{\mathbf{x}}_{c2} = \mathbf{A}_b\mathbf{x}_{c2} + \mathbf{B}_{b1}\mathbf{I}_s + \mathbf{B}_{b2}\mathbf{I}_{ref} \\ \mathbf{U}_o = \mathbf{C}_b\mathbf{x}_{c2} + \mathbf{D}_{b1}\mathbf{I}_s + \mathbf{D}_{b2}\mathbf{I}_{ref} \end{cases} \tag{10}$$

where $\mathbf{A}_b = 0$, $\mathbf{B}_{b1} = \begin{bmatrix} -K_i & 0 \\ 0 & -K_i \end{bmatrix}$, $\mathbf{B}_{b2} = \begin{bmatrix} K_i & 0 \\ 0 & K_i \end{bmatrix}$, $\mathbf{C}_b = \begin{bmatrix} 1 & 0 \\ 0 & 1 \end{bmatrix}$, $\mathbf{D}_{b1} = \begin{bmatrix} -K_{pd} & -L_q\omega_e \\ L_d\omega_e & -K_{pq} \end{bmatrix}$, $\mathbf{D}_{b2} = \begin{bmatrix} K_{pd} & 0 \\ 0 & K_{pq} \end{bmatrix}$.

Combining (5), (7), and (10), the whole system of feedback decoupling can be described as follows:

$$\begin{cases} \begin{bmatrix} \dot{\mathbf{x}}_{c2} \\ \dot{\mathbf{I}}_s \end{bmatrix} = \begin{bmatrix} \mathbf{A}_b & \mathbf{B}_{b1} \\ \mathbf{B}_m\mathbf{C}_b & \mathbf{A}_m + \mathbf{B}_m\mathbf{D}_{b1} \end{bmatrix} \begin{bmatrix} \mathbf{x}_{c2} \\ \mathbf{I}_s \end{bmatrix} + \begin{bmatrix} \mathbf{B}_{b2} \\ \mathbf{B}_m\mathbf{D}_{b2} \end{bmatrix} \mathbf{I}_{ref} \\ \mathbf{I}_s = \begin{bmatrix} 0 & \mathbf{I} \end{bmatrix} \begin{bmatrix} \mathbf{x}_{c2} \\ \mathbf{I}_s \end{bmatrix} \end{cases} \tag{11}$$

### *4.3. Internal Model Control Decoupling*

IMC decoupling introduces the motor model into the controller and regards the coupling terms as an internal dynamics section. Thus, decoupling is achieved within the controller. A filter connected in series with the inverse model prevents it from introducing too much hardware noise. Through transformation, the structure diagram is shown in Figure 3.

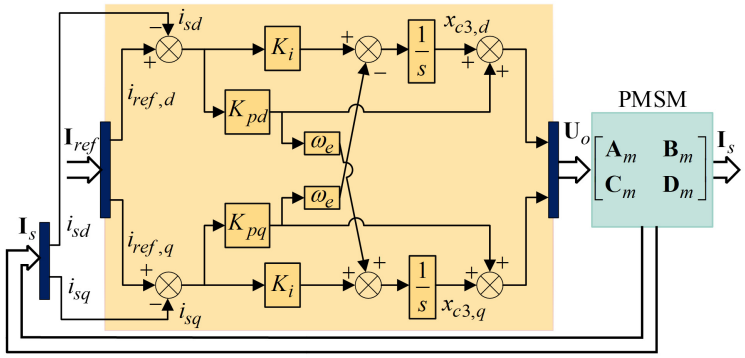



**Figure 3.** Structure diagram of IMC decoupling.

The state-space model of the IMC decoupling controller can be expressed as follows:

$$\begin{cases} \dot{\mathbf{x}}_{c3} = \mathbf{A}_{IMC}\mathbf{x}_{c3} + \mathbf{B}_{IMC1}\mathbf{I}_s + \mathbf{B}_{IMC2}\mathbf{I}_{ref} \\ \mathbf{U}_o = \mathbf{C}_{IMC}\mathbf{x}_{c3} + \mathbf{D}_{IMC1}\mathbf{I}_s + \mathbf{D}_{IMC2}\mathbf{I}_{ref} \end{cases} \tag{12}$$

where $\mathbf{A}_{IMC} = 0$, $\mathbf{B}_{IMC} = \begin{bmatrix} -K_i & \omega_e K_{pq} \\ -\omega_e K_{pd} & -K_i \end{bmatrix}$, $\mathbf{C}_{IMC} = \begin{bmatrix} 1 & 0 \\ 0 & 1 \end{bmatrix}$, $\mathbf{D}_{IMC1} = \begin{bmatrix} -K_{pd} & 0 \\ 0 & -K_{pq} \end{bmatrix}$, $\mathbf{D}_{IMC2} = \begin{bmatrix} K_{pd} & 0 \\ 0 & K_{pq} \end{bmatrix}$.

Combining (5), (7), and (12), the whole system can be expressed as follows:

$$\begin{cases} \begin{bmatrix} \dot{\mathbf{x}}_{c3} \\ \dot{\mathbf{I}}_s \end{bmatrix} = \begin{bmatrix} \mathbf{A}_{IMC} & \mathbf{B}_{IMC1} \\ \mathbf{B}_m\mathbf{C}_{IMC} & \mathbf{A}_m + \mathbf{B}_m\mathbf{D}_{IMC1} \end{bmatrix} \begin{bmatrix} \mathbf{x}_{c3} \\ \mathbf{I}_s \end{bmatrix} + \begin{bmatrix} \mathbf{B}_{IMC2} \\ \mathbf{B}_m\mathbf{D}_{IMC2} \end{bmatrix} \mathbf{I}_{ref} \\ \mathbf{I}_s = \begin{bmatrix} 0 & \mathbf{I} \end{bmatrix} \begin{bmatrix} \mathbf{x}_{c3} \\ \mathbf{I}_s \end{bmatrix} \end{cases} \tag{13}$$

## 5. Analysis of Current Decoupling Control Effect Based on Singular Value

In this section, we analyze the impact of rotor speed, estimation accuracy of stator inductance, and time delay on decoupling effectiveness. Comparisons of decoupling controllers introduced above are also conducted. Parameters of the system are shown in Table 2. Since the coupling effect is more pronounced at low bandwidths, the bandwidth used in this paper is relatively low for better comparison. Based on the motor specifications, the rated speed is theoretically approximately 250 Hz. The selected test points represent

20%, 40%, and 60% of the base speed. This establishes a progressive gradient covering the low-to-medium-high operating range. For frequency-domain evaluation, the singular values are expressed in decibels as follows:

$$\sigma_{dB} = 20log_{10}\,\sigma \tag{14}$$

**Table 2.** Parameters of the system.

| Parameter | Value |
|---|---|
| Rated power/kW | 1 |
| Rated speed/rpm | 3000 |
| Rated torque/Nm | 3.2 |
| Rated current/A | 6.5 |
| DC bus voltage/V | 48 |
| Inverter switching frequency/kHz | 10 |
| Sampling time/μs | 100 |
| Stator resistance/Ω | 0.92 |
| D-axis inductance/H | 0.002522 |
| Q-axis inductance/H | 0.00384 |
| Flux linkage/Wb | 0.057678 |
| Pole pairs | 5 |
| Control bandwidth/Hz | 300 |

### *5.1. Analysis of Decoupled Control Performance Under Speed and Parameter Deviations*

Considering that the coupling terms are proportional to both rotational speed and inductance magnitude, we analyze the effects of rotor speed and parameter accuracy on the decoupling and control performance. Based on the state-space equations, the images of the singular values in the frequency domain for each decoupled control system are plotted in Figure 4. When adopting a feedforward decoupling strategy, a distance between the maximum singular value and the minimum singular value exists, indicating the presence of coupling. As the speed gets higher, the distance grows further. The condition number is about 2.9 dB at 50 Hz, while it is 3.4 dB at 100 Hz and increases to 4.7 dB at 150 Hz. The maximum singular value increases at medium-to-high frequencies, exhibiting a trend of peak response. It is noted that an error between the reference current and stator current is invariably present at the moment when the reference signal is input, so feedforward decoupling cannot achieve complete dynamic decoupling. In Figure 4b,c, plots under different speeds are the same and the curves of maximum and minimum singular values coincide. This means both feedback and IMC decoupling controllers can eliminate coupling completely. And their performances are not influenced by rising rotor speed under this condition.

Accurate knowledge of the electrical parameters, like stator inductances of the dq-axis, is indispensable to achieve high-performance control [27,28]. However, parameter deviation occurs due to factors such as temperature and magnetic saturation. The actual inductance values decrease during operation [29]. Figure 5 shows the singular value plot at $\omega_e$ = 100 Hz, where the relationship between the actual and estimated values of the dq-axis inductance is given by $\hat{L}_{dq}$ =1.5 $L_{dq}$.

The singular values of all decoupling strategies shift to the right near the frequency of the control bandwidth, indicating an increase in closed-loop rise speed. For feedback and feedforward decoupling, the minimum singular value curve shifts downward, lower than 0 dB in the low-to-mid frequency range. Unlike when estimation is perfect, the two curves separate when feedback and IMC decoupling are adopted. Still, the separation

level of IMC decoupling is lower than that of feedback decoupling and is relatively small, demonstrating a lower sensitivity to parameter deviation.

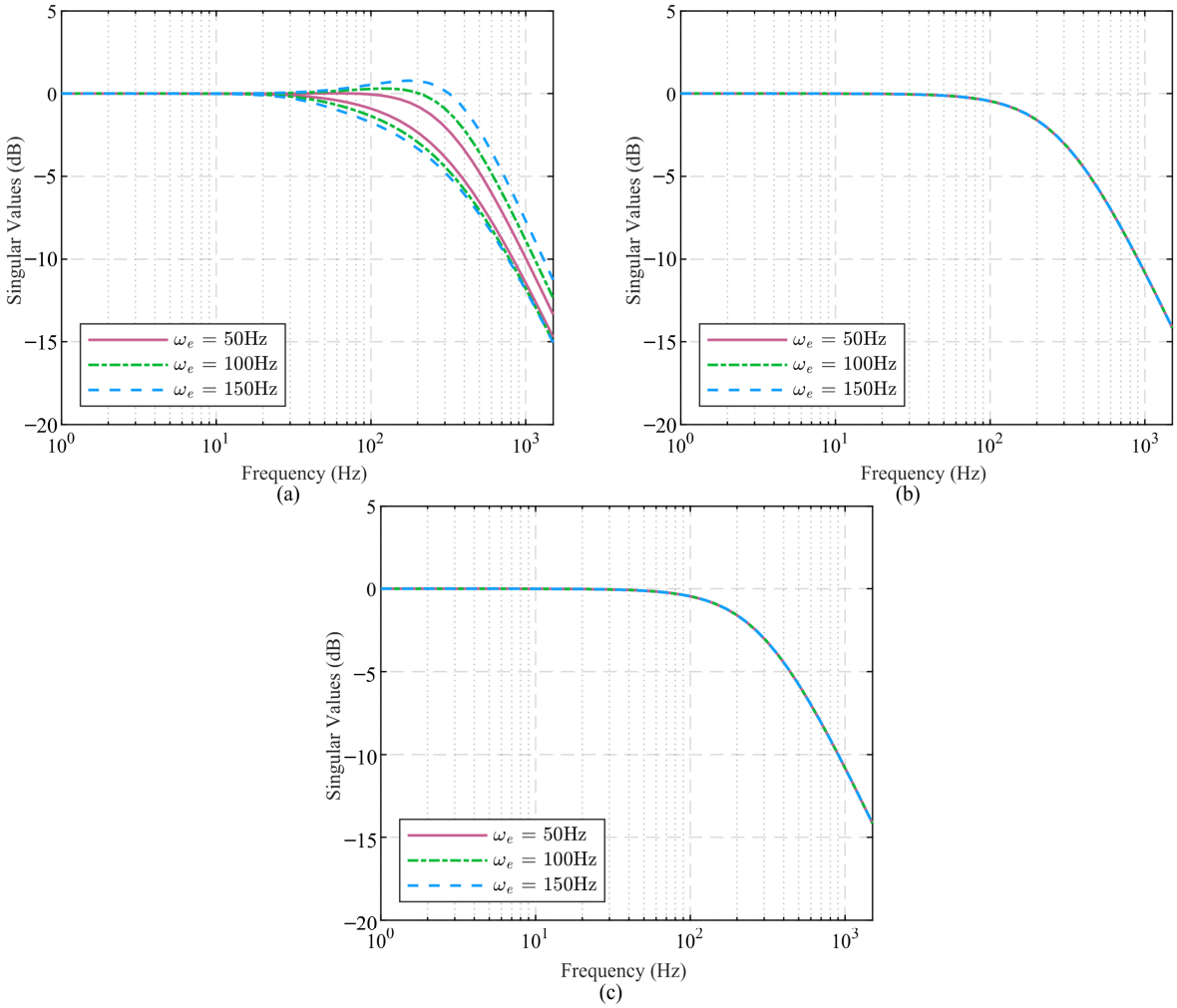



**Figure 4.** Singular value plot of the system without delay effects when parameter estimation is accurate. (**a**) Feedforward decoupling. (**b**) Feedback decoupling. (**c**) IMC decoupling.

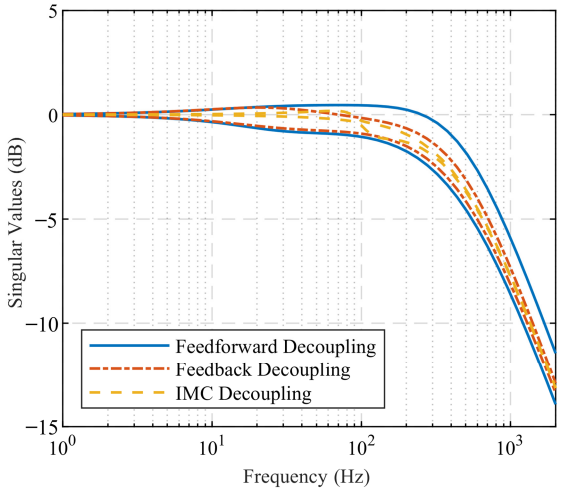



**Figure 5.** Singular value plot of the system without delay effects when $\omega_e$ =100 Hz, $\hat{L}_{dq}$ =1.5 $L_{dq}$.

*5.2. Analysis of Decoupled Control Performance Under Time Delay*

Digital control systems inevitably exhibit control lag due to processes such as time-consuming current sampling, calculations, and PWM output. This time delay results in rotor angular position error that causes phase and magnitude errors in the output value [30], along with a higher coupling condition. The overall system control block diagram is shown in Figure 6, and the delay segment is indicated in the blue dashed block. $T_d$ represents the delay time, whose optimal value can be determined to be 1.5 times the sampling period *Ts* through analysis and phase compensation in [31]. $\theta_D$ denotes the angle $\omega_e T_d$ rotated by the synchronous frame during the delay period. $K_D$ indicates the voltage amplitude gain, generally calculated using the average value [31]:

$$K_D = \frac{2}{T_s \omega_e} \sin\left(\frac{T_s \omega_e}{2}\right) \tag{15}$$

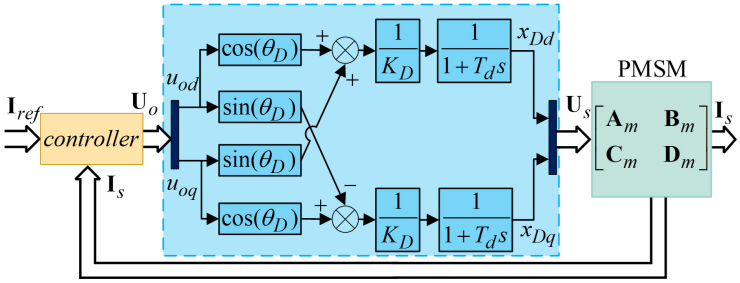



**Figure 6.** Diagram of the control system including time delay.

By defining the system input as $U_o = [u_{od}\ u_{oq}]^T$, the output as $U_s = [u_{sd}\ u_{sq}]^T$, and the system state as $\boldsymbol{x}_D = [x_{Dd}\ x_{Dq}]^T$, the state-space of the delay segment can be formulated as follows:

$$\begin{cases} \dot{\mathbf{x}}_D = \mathbf{A}_D \mathbf{x}_D + \mathbf{B}_D \mathbf{U}_o \\ \mathbf{U}_s = \mathbf{C}_D \mathbf{x}_D \end{cases} \tag{16}$$

where $\mathbf{A}_D = -\frac{1}{T_d}\begin{bmatrix} 1 & 0 \\ 0 & 1 \end{bmatrix}$, $\mathbf{B}_D = \frac{1}{T_d K_D}\begin{bmatrix} \cos\theta_D & \sin\theta_D \\ -\sin\theta_D & \cos\theta_D \end{bmatrix}$, $\mathbf{C}_D = \begin{bmatrix} 1 & 0 \\ 0 & 1 \end{bmatrix}$.

Combining Equations (5) and (15) with the controller state-space Equations (8), (10) and (12), we yield the overall state-space control formula incorporating time delays:

$$\begin{cases} \begin{bmatrix} \dot{\mathbf{x}}_c \\ \dot{\mathbf{x}}_D \\ \dot{\mathbf{I}}_s \end{bmatrix} = \begin{bmatrix} \mathbf{A}_c & 0 & \mathbf{B}_{c1} \\ \mathbf{B}_D \mathbf{C}_c & \mathbf{A}_D & \mathbf{B}_D \mathbf{D}_{c1} \\ 0 & \mathbf{B}_m \mathbf{C}_D & \mathbf{A}_m \end{bmatrix} \begin{bmatrix} \mathbf{x}_c \\ \mathbf{x}_D \\ \mathbf{I}_s \end{bmatrix} + \begin{bmatrix} \mathbf{B}_{c2} \\ \mathbf{B}_D \mathbf{D}_{c2} \\ 0 \end{bmatrix} \mathbf{I}_{ref} \\ \mathbf{I}_s = \begin{bmatrix} 0 & 0 & \mathbf{I} \end{bmatrix} \begin{bmatrix} \mathbf{x}_c \\ \mathbf{x}_D \\ \mathbf{I}_s \end{bmatrix} \end{cases} \tag{17}$$

where $\mathbf{A}_c$, $\boldsymbol{B}_{c1}$, $\boldsymbol{B}_{c2}$, $\boldsymbol{D}_{c1}$, $\boldsymbol{D}_{c2}$ denote the controller matrix coefficients.

When the sampling time remains unchanged, the extent of the delay effect is directly related to rotor speed. This part analyzes the decoupling performance influenced by time delay under different speeds. Based on (16), the singular value plot of each decoupling system is shown in Figure 7.

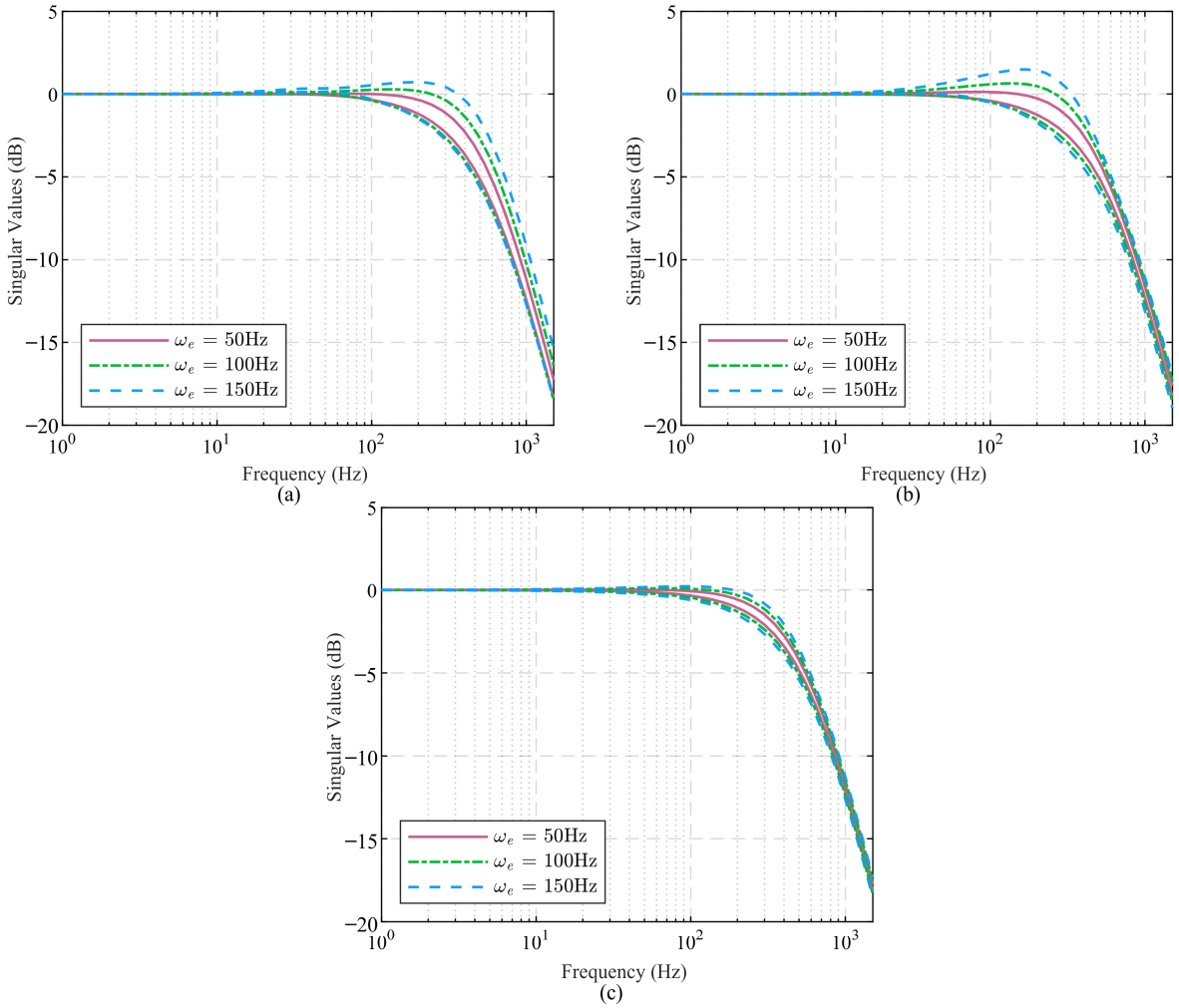



**Figure 7.** Singular value plot of the system with delay effects when parameter estimation is accurate. (**a**) Feedforward decoupling. (**b**) Feedback decoupling. (**c**) IMC decoupling.

Then we compare plots at the same speed between Figures 4 and 7. For feedforward decoupling, both the curves of maximum and minimum singular values shift upward near the frequency of the control bandwidth, while the curve of minimum singular value shifts a little more. Thus, the distance between them slightly decreases, indicating that delay has a relatively minor impact on this strategy. But the system still exhibits significant coupling due to the existence of the error between reference current and stator current at the moment when the reference signal is input.

For feedback decoupling, the two curves separate, and the maximum singular value curve moves upward. As the speed gets higher, there is an increasing peak response, which reaches 1.50 dB at a speed of 150 Hz. In that case, the decoupling performance is degraded, along with a deteriorated dynamic response. It can then be inferred that feedback decoupling is highly sensitive to digital delay. For IMC decoupling, there is also coupling content. However, the separation of singular value plots at different rotor speeds is lower. That is, IMC decoupling is less sensitive to digital time delay.

## 6. Simulation and Experiment

### *6.1. Simulation*

To verify the theoretical analysis, simulations are conducted based on Simulink. Parameters are shown in Table 2. In the model where the counter-electromotive force is assumed to be fully compensated and parameters are tuned based on zero–pole cancella-

tion, the primary distinction in the dq-axis voltage lies in the differing magnitudes of the inductance in the coupling terms. Hence, the validation is undertaken through a step in q-axis current.

The q-axis current steps to 8 A at 0.02 s. When parameter estimation is accurate, simulation results of the dq-axis currents without delay effects are shown in Figure 8. Simulation results of three-phase currents are also provided in Figure 9.

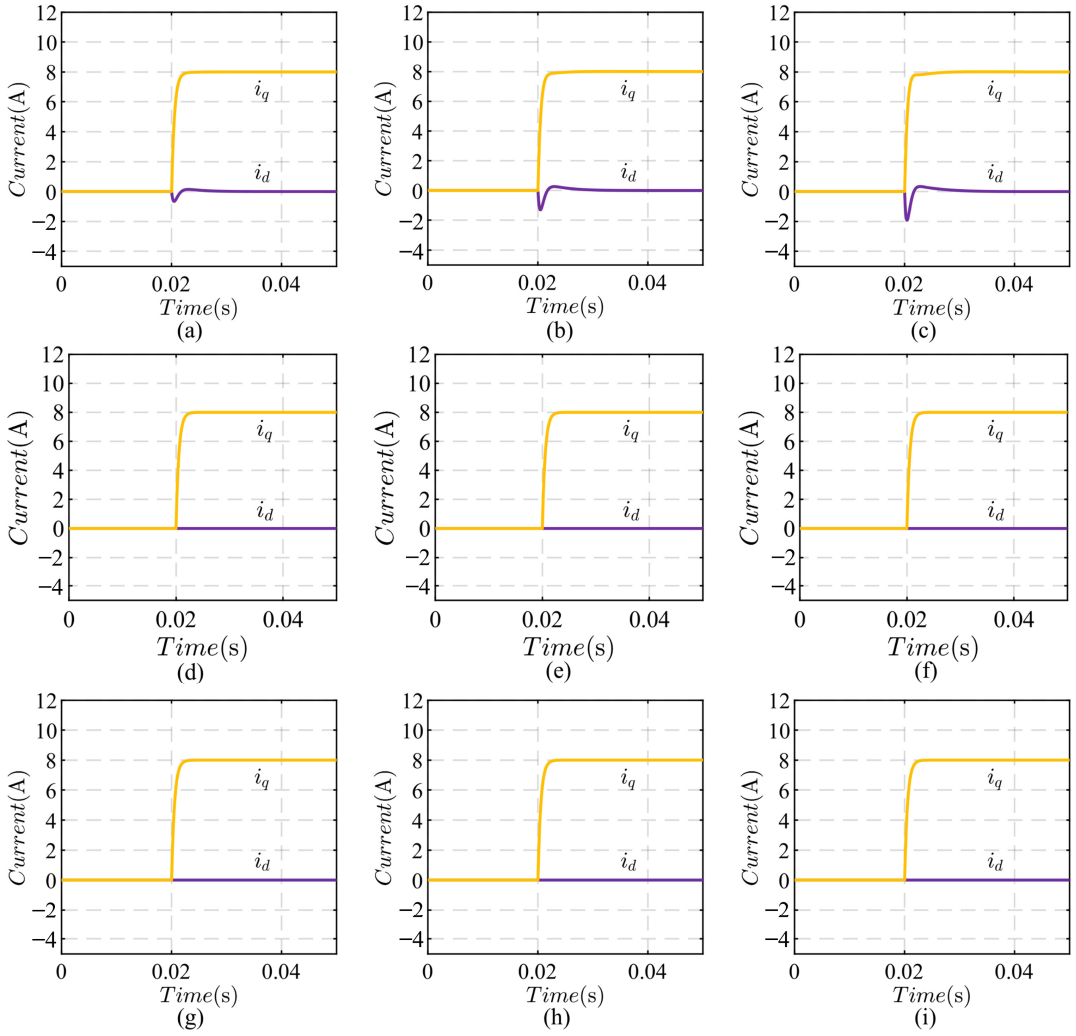



**Figure 8.** Simulation results of dq-axis currents without delay effects when parameter estimation is accurate. (**a**) Feedforward decoupling at $\omega_e$ = 50 Hz. (**b**) Feedforward decoupling at $\omega_e$ = 100 Hz. (**c**) Feedforward decoupling at $\omega_e$ = 150 Hz. (**d**) Feedback decoupling at $\omega_e$ = 50 Hz. (**e**) Feedback decoupling at $\omega_e$ = 100 Hz. (**f**) Feedback decoupling at $\omega_e$ = 150 Hz. (**g**) IMC decoupling at $\omega_e$ = 50 Hz. (**h**) IMC decoupling at $\omega_e$ = 100 Hz. (**i**) IMC decoupling at $\omega_e$ = 150 Hz.

For feedforward decoupling, owing to the coupling effect, the d-axis current varies as the q-axis current steps. This variation becomes more significant at higher speeds. For feedback and IMC decoupling, the d-axis current does not change, and the whole response curves are the same at different speeds. This is consistent with the analysis of the singular value plots.

When $\omega_e$ = 100 Hz and $\hat{L}_{dq}$ =1.5 $L_{dq}$, simulation results without delay effects are shown in Figures 10 and 11.

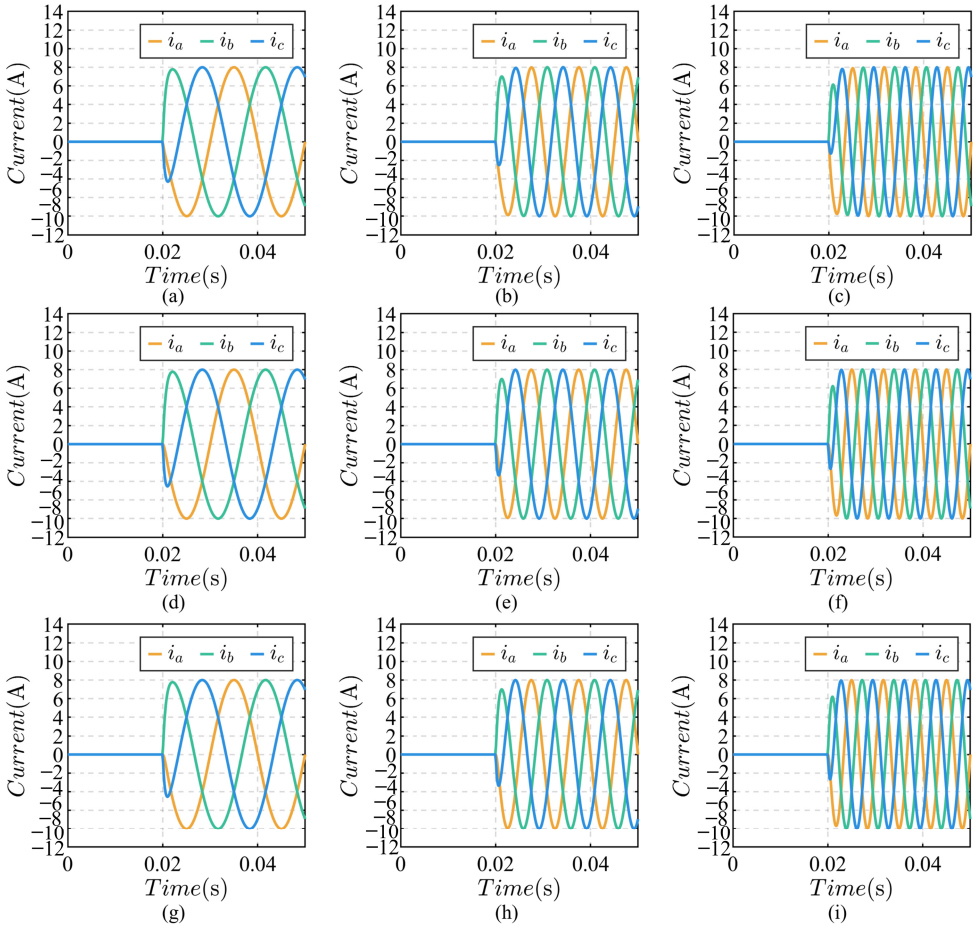



**Figure 9.** Simulation results of three-phase currents without delay effects when parameter estimation is accurate. (**a**) Feedforward decoupling at $\omega_e$ = 50 Hz. (**b**) Feedforward decoupling at $\omega_e$ = 100 Hz. (**c**) Feedforward decoupling at $\omega_e$ = 150 Hz. (**d**) Feedback decoupling at $\omega_e$ = 50 Hz. (**e**) Feedback decoupling at $\omega_e$ = 100 Hz. (**f**) Feedback decoupling at $\omega_e$ = 150 Hz. (**g**) IMC decoupling at $\omega_e$ = 50 Hz. (**h**) IMC decoupling at $\omega_e$ = 100 Hz. (**i**) IMC decoupling at $\omega_e$ = 150 Hz.

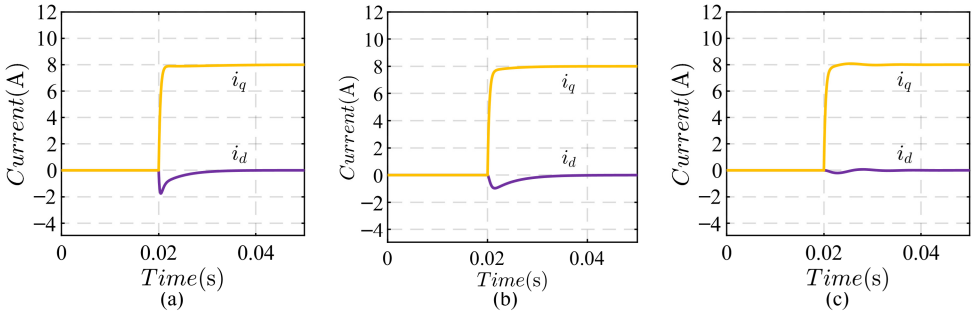



**Figure 10.** Simulation results of dq-axis currents without delay effects when $\omega_e$ = 100 Hz, $\hat{L}_{dq}$ = 1.5 $L_{dq}$. (**a**) Feedforward decoupling. (**b**) Feedback decoupling. (**c**) IMC decoupling.

The current reaches 95% of the reference value at a faster tracking speed for all strategies. But for feedback decoupling, the speed slows thereafter due to amplitude attenuation in the mid-frequency band. A noticeable decline of $i_d$ is also shown in Figure 10b since feedback decoupling degraded, as analyzed. Slightly influenced by the parameter deviation, IMC decoupling has stronger robustness, which corresponds to the lesser degree of separation between its two curves.

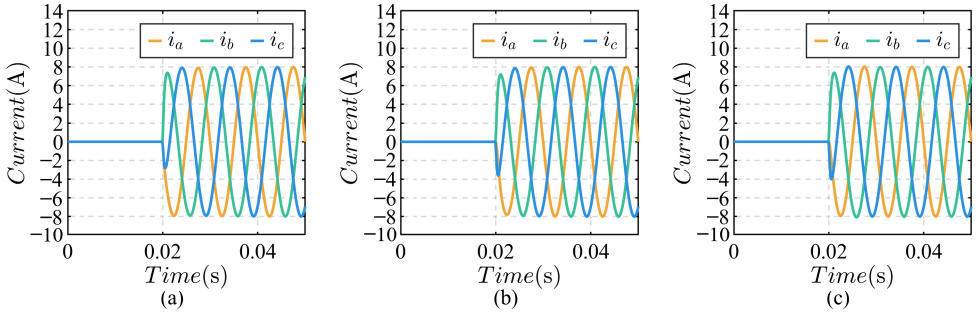



**Figure 11.** Simulation results of three-phase currents without delay effects when $\omega_e$ = 100 Hz, $\hat{L}_{dq}$ = 1.5 $L_{dq}$. (**a**) Feedforward decoupling. (**b**) Feedback decoupling. (**c**) IMC decoupling.

Simulation results with delay effects and accurate parameter estimation are shown in Figures 12 and 13.

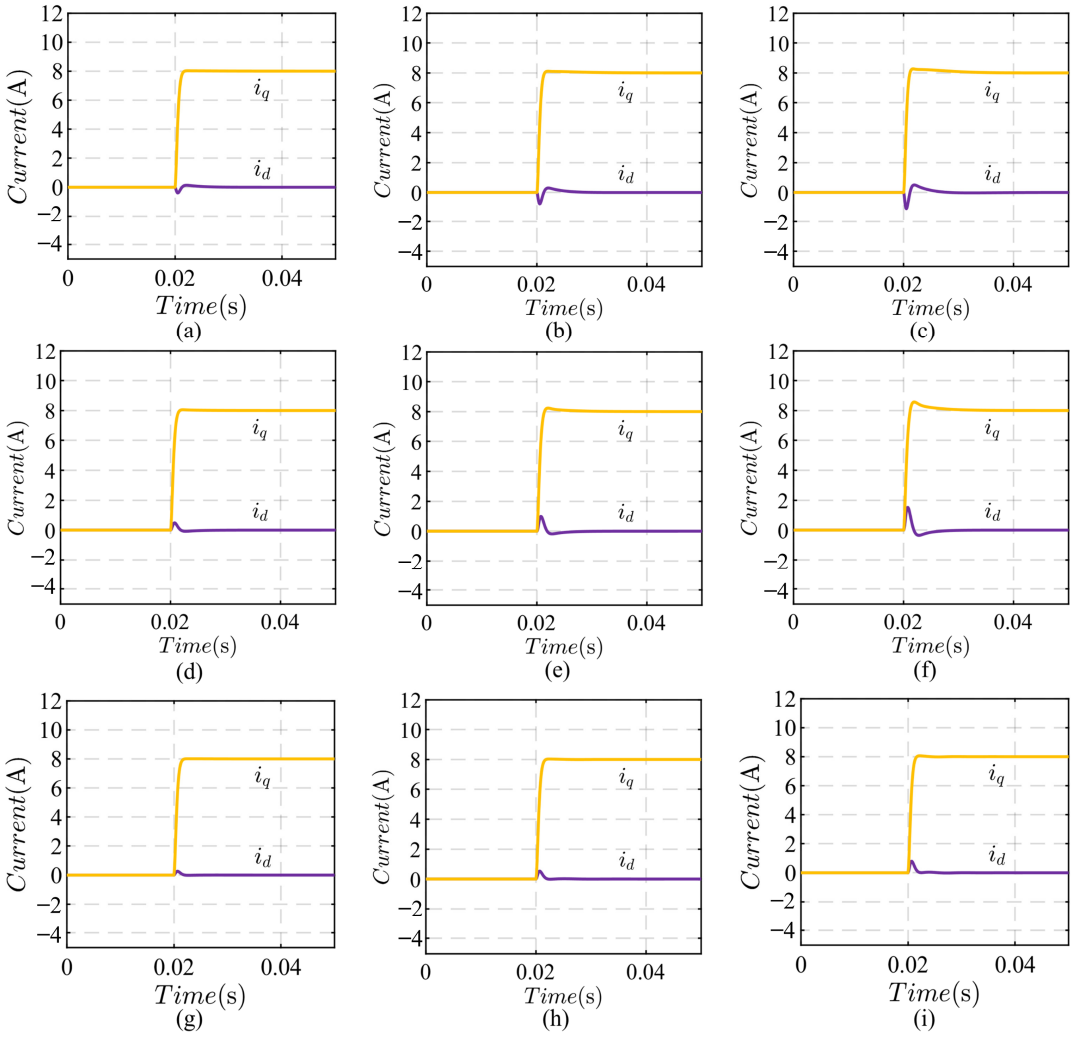



**Figure 12.** Simulation results of dq-axis currents with delay effects and accurate parameter estimation. (**a**) Feedforward decoupling at $\omega_e$ = 50 Hz. (**b**) Feedforward decoupling at $\omega_e$ = 100 Hz. (**c**) Feedforward decoupling at $\omega_e$ = 150 Hz. (**d**) Feedback decoupling at $\omega_e$ = 50 Hz. (**e**) Feedback decoupling at $\omega_e$ = 100 Hz. (**f**) Feedback decoupling at $\omega_e$ = 150 Hz. (**g**) IMC decoupling at $\omega_e$ = 50 Hz. (**h**) IMC decoupling at $\omega_e$ = 100 Hz. (**i**) IMC decoupling at $\omega_e$ = 150 Hz.

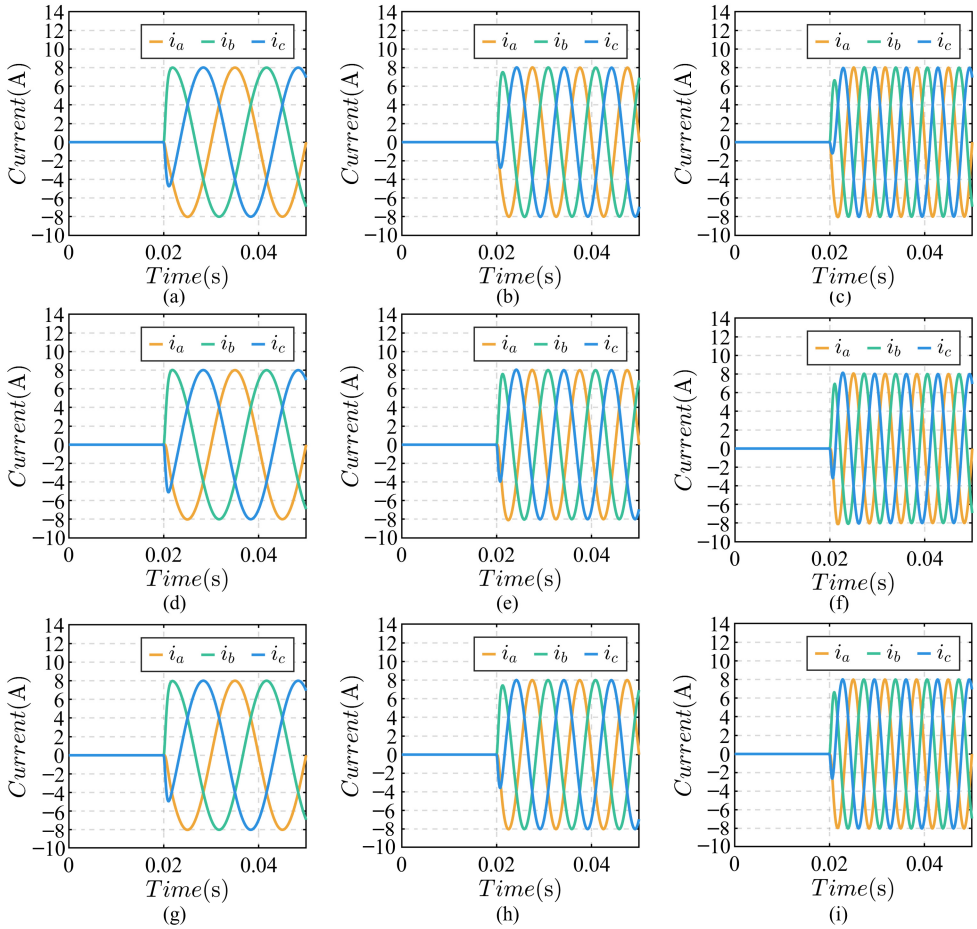



**Figure 13.** Simulation results of three-phase currents with delay effects and accurate parameter estimation. (**a**) Feedforward decoupling at $\omega_e$ = 50 Hz. (**b**) Feedforward decoupling at $\omega_e$ = 100 Hz. (**c**) Feedforward decoupling at $\omega_e$ = 150 Hz. (**d**) Feedback decoupling at $\omega_e$ = 50 Hz. (**e**) Feedback decoupling at $\omega_e$ = 100 Hz. (**f**) Feedback decoupling at $\omega_e$ = 150 Hz. (**g**) IMC decoupling at $\omega_e$ = 50 Hz. (**h**) IMC decoupling at $\omega_e$ = 100 Hz. (**i**) IMC decoupling at $\omega_e$ = 150 Hz.

For feedforward decoupling, the d-axis varies less than that in Figure 8. Still, its decoupling capability is limited as the speed gets higher. Feedback decoupling exhibits overshoot that increases with rising rotor speed. IMC decoupling varies the least, which is in accordance with the theoretical results.

### *6.2. Experiment*

The experimental validation is conducted on a back-to-back test bench, as depicted in Figure 14. One motor rotates at a specified speed and acts as a load, while the other motor, which we analyzed before, is given a step command on $i_q$. A rotation matrix is applied in the current loop to compensate for the angular error caused by time delay. The parameters used for the experiment are the same as those for simulation, as shown in Table 2.

The experimental results with delay compensation under perfect parameter estimation are shown in Figures 15 and 16. Since the delay effect may not be completely eliminated, the experimental images are not exactly the same as the simulation results, particularly for feedback decoupling, which is highly sensitive to delays.

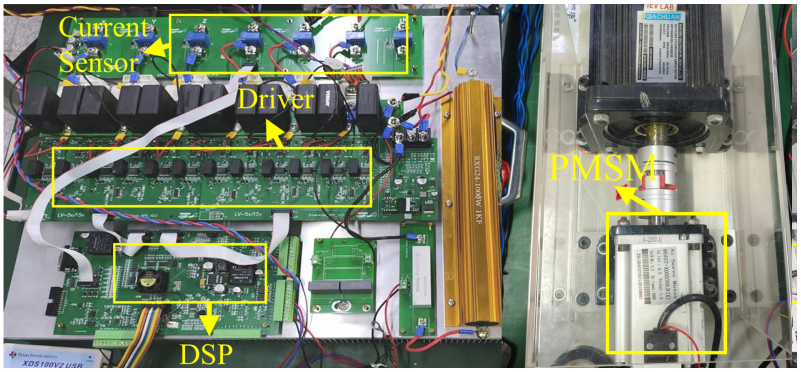



**Figure 14.** Experimental platform.

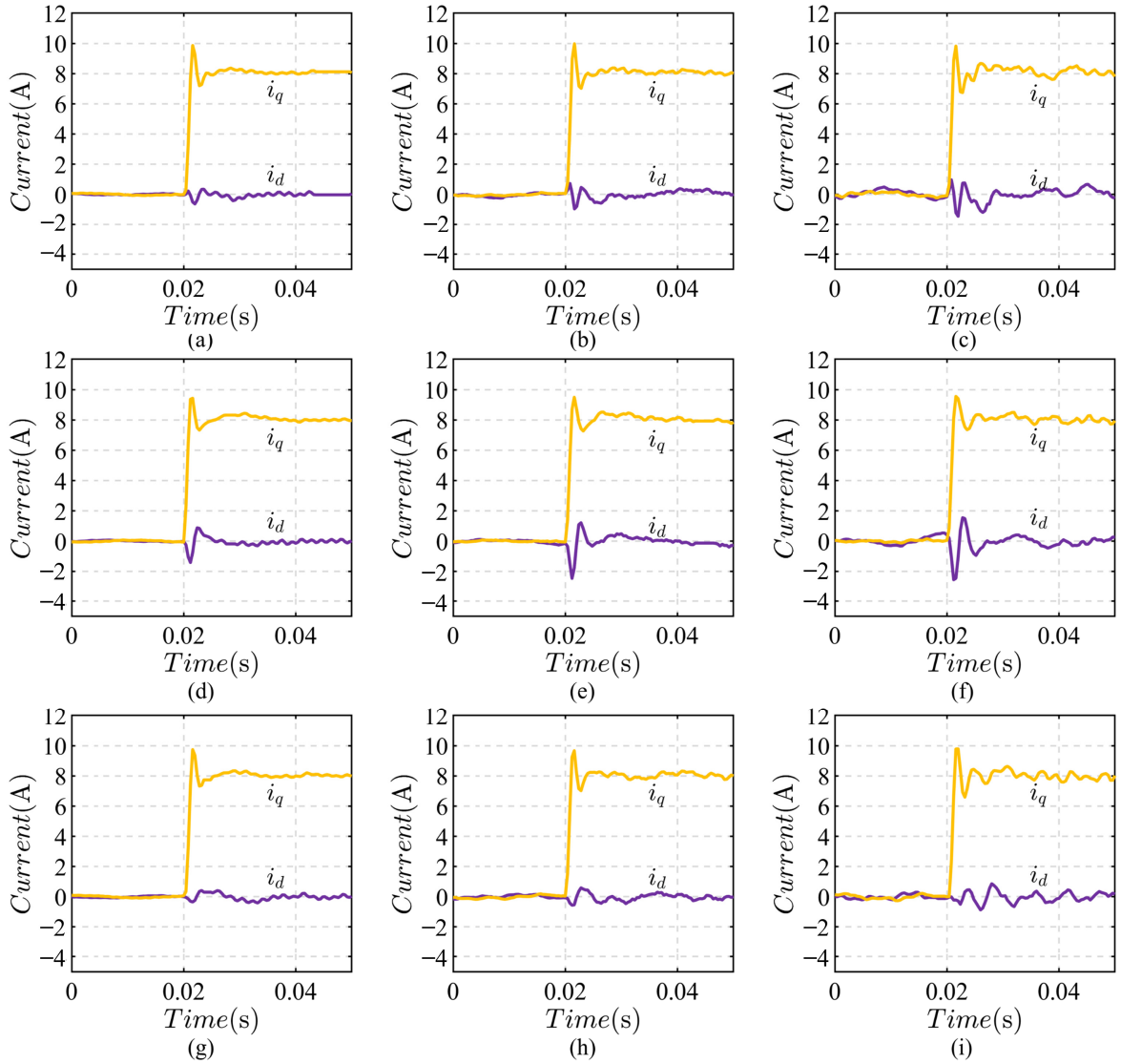



**Figure 15.** Experimental results of dq-axis currents with delay compensation when parameter estimation is accurate. (**a**) Feedforward decoupling at $\omega_e$ = 50 Hz. (**b**) Feedforward decoupling at $\omega_e$ = 100 Hz. (**c**) Feedforward decoupling at $\omega_e$ = 150 Hz. (**d**) Feedback decoupling at $\omega_e$ = 50 Hz. (**e**) Feedback decoupling at $\omega_e$ = 100 Hz. (**f**) Feedback decoupling at $\omega_e$ = 150 Hz. (**g**) IMC decoupling at $\omega_e$ = 50 Hz. (**h**) IMC decoupling at $\omega_e$ = 100 Hz. (**i**) IMC decoupling at $\omega_e$ = 150 Hz.

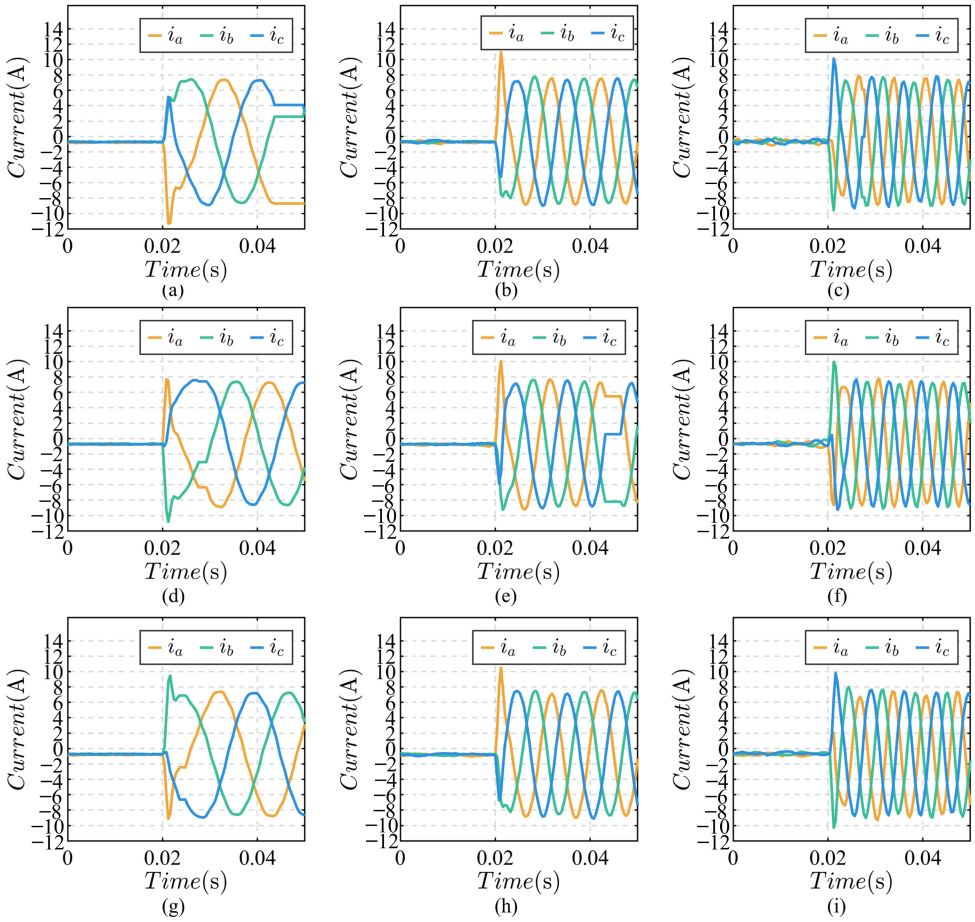



**Figure 16.** Experimental results of three-phase currents with delay compensation when parameter estimation is accurate. (**a**) Feedforward decoupling at $\omega_e$ = 50 Hz. (**b**) Feedforward decoupling at $\omega_e$ = 100 Hz. (**c**) Feedforward decoupling at $\omega_e$ = 150 Hz. (**d**) Feedback decoupling at $\omega_e$ = 50 Hz. (**e**) Feedback decoupling at $\omega_e$ = 100 Hz. (**f**) Feedback decoupling at $\omega_e$ = 150 Hz. (**g**) IMC decoupling at $\omega_e$ = 50 Hz. (**h**) IMC decoupling at $\omega_e$ = 100 Hz. (**i**) IMC decoupling at $\omega_e$ = 150 Hz.

Figures 17 and 18 show the experimental results when $\omega_e$ = 100 Hz, $\hat{L}_{dq}$ = 1.5 $L_{dq}$. Compared with results under perfect parameter estimation, the maximum variation of $i_d$ due to coupling increases by about 62.1% for feedforward decoupling. This is about 18.9% for IMC decoupling and about 14.7% for feedback decoupling. The value for feedback decoupling is close to that for internal model decoupling and much smaller than that for feedforward decoupling, which is consistent with theoretical and simulation analyses. IMC decoupling exhibits stronger robustness.

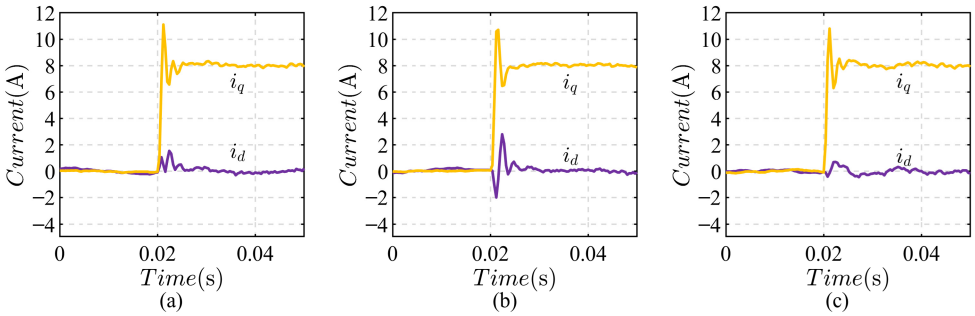



**Figure 17.** Experimental results of dq-axis currents without delay effects when $\omega_e$ = 100 Hz, $\hat{L}_{dq}$ = 1.5 $L_{dq}$. (**a**) Feedforward decoupling. (**b**) Feedback decoupling. (**c**) IMC decoupling.

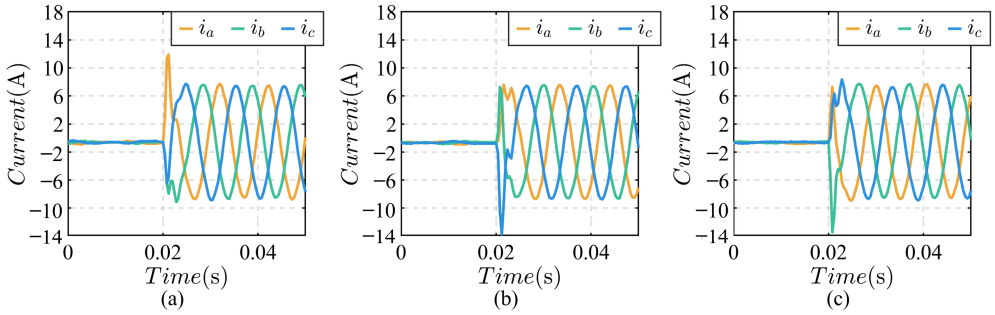



**Figure 18.** Experimental results of three-phase currents without delay effects when $\omega_e$ = 100 Hz, $\hat{L}_{dq}$ = 1.5 $L_{dq}$. (**a**) Feedforward decoupling. (**b**) Feedback decoupling. (**c**) IMC decoupling.

Experimental results without compensation of time delay are shown in Figures 19 and 20. The waveform of feedback decoupling exhibits greater overshoot and coupling due to the delay effect. Compared with Figure 15, when $\omega_e$ = 150 Hz, under the feedback decoupling strategy, the system's overshoot rate surges from 19.4% to 33.4%, and the overshoot magnitude increases by 72.2%. For feedforward decoupling, the system's overshoot rate increases by 24.3%, while the maximum variation of $i_d$ slightly reduces from 1.45 A to 1.39 A. For IMC decoupling, the system's overshoot rate only increases by 7.6%, and the maximum variation of $i_d$ is still relatively low. A quantitative comparison of experimental results under three decoupling strategies is shown in Table 3.

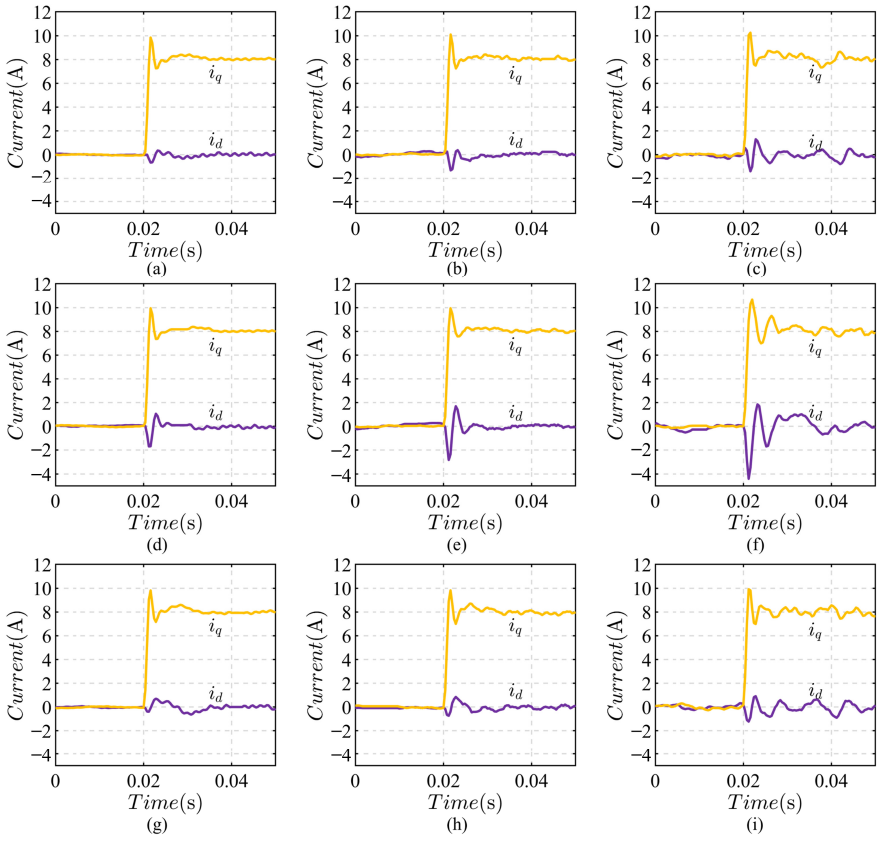



**Figure 19.** Experimental results of dq-axis currents without delay compensation when parameter estimation is accurate. (**a**) Feedforward decoupling at $\omega_e$ = 50 Hz. (**b**) Feedforward decoupling at $\omega_e$ = 100 Hz. (**c**) Feedforward decoupling at $\omega_e$ = 150 Hz. (**d**) Feedback decoupling at $\omega_e$ = 50 Hz. (**e**) Feedback decoupling at $\omega_e$ = 100 Hz. (**f**) Feedback decoupling at $\omega_e$ = 150 Hz. (**g**) IMC decoupling at $\omega_e$ = 50 Hz. (**h**) IMC decoupling at $\omega_e$ = 100 Hz. (**i**) IMC decoupling at $\omega_e$ = 150 Hz.

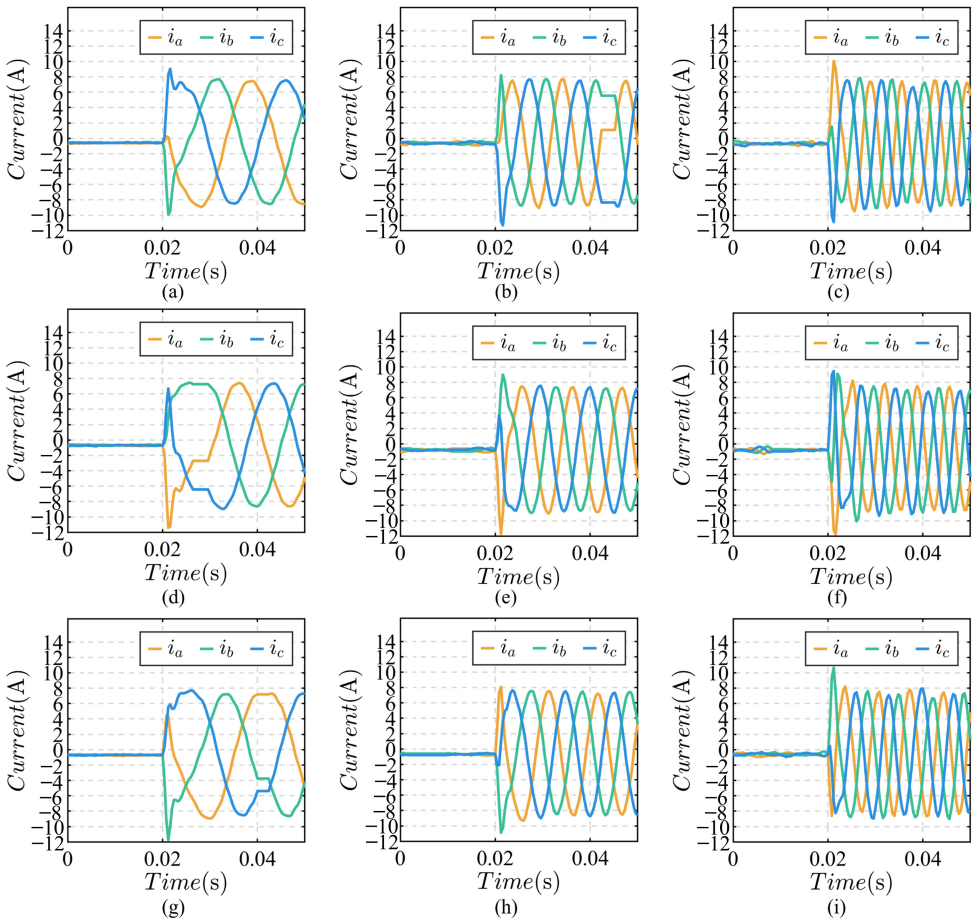



**Figure 20.** Experimental results of three-phase currents without delay compensation when parameter estimation is accurate. (**a**) Feedforward decoupling at $\omega_e$ = 50 Hz. (**b**) Feedforward decoupling at $\omega_e$ = 100 Hz. (**c**) Feedforward decoupling at $\omega_e$ = 150 Hz. (**d**) Feedback decoupling at $\omega_e$ = 50 Hz. (**e**) Feedback decoupling at $\omega_e$ = 100 Hz. (**f**) Feedback decoupling at $\omega_e$ = 150 Hz. (**g**) IMC decoupling at $\omega_e$ = 50 Hz. (**h**) IMC decoupling at $\omega_e$ = 100 Hz. (**i**) IMC decoupling at $\omega_e$ = 150 Hz.

**Table 3.** Quantitative comparison of experimental results under three decoupling strategies.

| Decoupling Strategy | Rotor Speed (Hz) | Nominal Condition | | Parameter Mismatch | | Delay Effect | |
|---|---|---|---|---|---|---|---|
| | | Overshoot (%) | $i_d$ Variation (A) | Overshoot (%) | $i_d$ Variation (A) | Overshoot (%) | $i_d$ Variation (A) |
| Feedforward | 50 | 23.1 | 0.62 | 38.9 | 1.54 | 23.0 | 0.64 |
| | 100 | 24.6 | 0.95 | | | 26.2 | 1.31 |
| | 150 | 22.6 | 1.45 | | | 28.0 | 1.39 |
| Feedback | 50 | 17.8 | 1.39 | 33.9 | 2.80 | 24.3 | 1.68 |
| | 100 | 18.6 | 2.45 | | | 24.3 | 2.82 |
| | 150 | 19.4 | 2.53 | | | 33.4 | 4.41 |
| IMC | 50 | 21.6 | 0.35 | 35.0 | 0.69 | 22.5 | 0.70 |
| | 100 | 20.8 | 0.58 | | | 22.7 | 0.85 |
| | 150 | 22.1 | 0.87 | | | 23.9 | 1.22 |

The results indicate that the coupling degree exhibits a substantial increase in proportion to an increase in rotor speed. This verifies the singular value analysis and simulation results of the impact of time delay. The superior performance of the IMC strategy, as observed in the results, can mainly be attributed to its structural advantages. It uses an internal model in parallel with the controlled system, taking cross-coupling into ac-

count. Both feedforward decoupling and feedback decoupling consider decoupling as an anti-disturbance problem of the SISO system. Thus, they can be seen as traditional PI controllers that independently control each current internally while incorporating external compensation. For feedforward decoupling, it can achieve complete decoupling when the current reaches the reference value, so its decoupling effectiveness is related to the tracking capability. Moreover, the open-loop compensation method determines its high parameter sensitivity. As for feedback decoupling, it depends on the motor to generate the decoupling term; thus, it is more sensitive to delay effects. Still, there exist unmodeled dynamics and physical constraints in the experiments. On top of that, the proposed analysis is based on a linearized current-loop model of a permanent magnet synchronous motor centered on a specific operating point and may not fully reflect all nonlinear effects in actual permanent magnet synchronous motors, which may cause discrepancies.

## 7. Conclusions

Addressing the problem of evaluating the effectiveness of current decoupling controllers for PMSMs, this paper introduces frequency-domain singular values as a graphical analysis tool. By plotting singular value curves, system coupling trends and magnitude–frequency response characteristics of different controllers are analyzed more intuitively. In the absence of time-delay effects, feedback decoupling and internal model control decoupling can fully decouple and are unaffected by rotor speed. However, the impact of digital delay intensifies with higher rotor speed. Feedback decoupling is highly sensitive to digital time delay, leading to deterioration in control performance. Feedforward decoupling offers minor enhancement of decoupling in the context of time delay, but the system continues to exhibit a substantial degree of coupling, primarily attributable to the high rotor speed. In contrast, internal model control decoupling has stronger robustness. Subsequent analyses incorporating the delay effect alongside parameter estimation error would better approximate real-world conditions, especially at high rotor speed. Simulation and experimental results have validated the validity and feasibility of this analysis. Although this paper takes an automotive drive motor scenario as a case study, it can be applied to other linear time-invariant PMSM systems adopting FOC, which operate around a steady-state operating point. In practice, systems rarely achieve full compensation; assuming that the permanent magnet back-EMF disturbance has been fully compensated may exclude a physical source of coupling from the analysis. It should also be noted that this method cannot evaluate stability. Therefore, combining it with stability analysis methods will provide a more comprehensive assessment of the control system's performance.

**Author Contributions:** Conceptualization, T.Z. and Q.L.; methodology, Q.L.; software, P.X., H.Z. and J.Z.; validation, T.Z., H.Z. and J.Z.; formal analysis, T.Z.; writing—original draft preparation, T.Z.; writing—review and editing, T.Z.; supervision, Q.L.; funding acquisition, Q.L. and D.W. All authors have read and agreed to the published version of the manuscript.

**Funding:** This research was funded in part by the Shandong Natural Science Foundation of Young Scientists Fund under grant number ZR2024QE117, in part by the National Natural Science Foundation of China Young Scientists Fund, grant number 52402512, and in part by the Shandong Key Research and Development Plan Fund, grant number 2024ZLGX11.

**Data Availability Statement:** The original contributions presented in this study are included in the article. Further inquiries can be directed to the corresponding author.

**Conflicts of Interest:** The authors declare no conflicts of interest.

## References


1. Sun, J.; Yang, Y.; Chen, R.; Zhang, X.; Lim, C.S.; Rodriguez, J. An efficient multi-vector-based model predictive current control for PMSM drive. *CPSS Trans. Power Electron. Appl.* **2023**, *9*, 79–89. [CrossRef]
2. Zhang, R.; Yin, Z.; Liu, J.; Yu, S. Low carrier wave ratio modulation strategy of permanent magnet synchronous motor based on metro traction system: A comparative study. *CPSS Trans. Power Electron. Appl.* **2022**, *7*, 1–16. [CrossRef]
3. El Hajji, T.; Hlioui, S.; Louf, F.; Gabsi, M.; Mermaz-Rollet, G.; Belhadi, M.H. Optimal design of high-speed electric machines for electric vehicles: A case study of 100 kW V-shaped interior PMSM. *Machines* **2023**, *11*, 57. [CrossRef]
4. Rahman, S.U.; Xia, C. Rotor speed and position estimation analysis of interior PMSM machines in low and medium-high speed regions adopting an improved flux observer for electric vehicle applications. *Machines* **2023**, *11*, 574. [CrossRef]
5. Ilioudis, V.C. Sensorless control of permanent magnet synchronous machine with magnetic saliency tracking based on voltage signal injection. *Machines* **2020**, *8*, 14. [CrossRef]
6. Zheng, C.; Xie, M.; Dong, X.; Gong, Z.; Dragičević, T.; Rodriguez, J. Design and Analysis of Predictive Inductor Current Control for PMSM Drives With LC Filter. *IEEE Trans. Power Electron.* **2025**, *40*, 1872–1885. [CrossRef]
7. Yang, H.; Tao, L.; Wang, J.; Li, Z.; Zhou, L. Discrete-Time Speed-Independent Current Control for Zero Tracking Error in Low-Inertia PMSM Drives. *IEEE Trans. Ind. Electron.* **2026**, *73*, 11100–11112. [CrossRef]
8. Teymoori, V.; Ghalebani, P.; Kamper, M.J.; Wang, R.J.; Arish, N. Sensorless Adaptive PI Control of High-Power Propulsion PMSM Based on Sliding-Mode Extremum Seeking Algorithm With Variation Parameters. *IEEE Trans. Ind. Appl.* **2026**, *62*, 3908–3920. [CrossRef]
9. Hussain, H.A. Tuning and performance evaluation of 2DOF PI current controllers for PMSM drives. *IEEE Trans. Transp. Electrif.* **2020**, *7*, 1401–1414. [CrossRef]
10. Wang, Q.; Yang, S.; Xie, Z.; Zhang, X.; Chang, L. Two-degree-of-freedom discrete-time decoupled current control of IPMSM with high parameter robustness. *IEEE J. Emerg. Sel. Top. Power Electron.* **2024**, *12*, 4716–4727. [CrossRef]
11. Shi, C.; Tang, S.; Zhang, C.; Li, X.; Li, Y.; Yan, Y.; Shi, T. Current decoupling control for interior permanent magnet synchronous motor. *IEEE Trans. Energy Convers.* **2024**, *40*, 1578–1588. [CrossRef]
12. Zhu, Z.; Wang, X.; Yan, B.; Li, L.; Wu, Q. A dynamic decoupling control method for PMSM of brake-by-wire system based on parameters estimation. *IEEE/ASME Trans. Mechatron.* **2021**, *27*, 3762–3772. [CrossRef]
13. Yao, Y.; Huang, Y.; Peng, F.; Dong, J.; Zhu, Z. Dynamic-decoupled active damping control method for improving current transient behavior of LCL-equipped high-speed PMSMs. *IEEE Trans. Power Electron.* **2021**, *37*, 3259–3271. [CrossRef]
14. Wen, J.; Yuan, X.; Niu, S.; Chan, W.-L. A robust complex vector PI current controller with deadbeat response for PMSM drives. *IEEE Trans. Ind. Electron.* **2024**, *72*, 4671–4681. [CrossRef]
15. Pan, Y.; Liu, X.; Zhu, Y.; Liu, B.; Li, Z. Feedforward decoupling control of interior permanent magnet synchronous motor with genetic algorithm parameter identification. *Prog. Electromagn. Res. M* **2021**, *102*, 117–126. [CrossRef]
16. Zhou, S.; Liu, J.; Zhou, L.; Zhang, Y. DQ current control of voltage source converters with a decoupling method based on preprocessed reference current feed-forward. *IEEE Trans. Power Electron.* **2017**, *32*, 8904–8921. [CrossRef]
17. Petric, I.Z.; Vukosavic, S.N.; Degano, M.; Galassini, A. A digital internal model current controller for salient machines. *IEEE Trans. Ind. Electron.* **2020**, *68*, 4703–4717. [CrossRef]
18. Jung, J.; Nam, K. A dynamic decoupling control scheme for high-speed operation of induction motors. *IEEE Trans. Ind. Electron.* **1999**, *46*, 100–110. [CrossRef]
19. Diab, A.M.; Guo, F.; Yeoh, S.S.; Bozhko, S.; Gerada, C.; Galea, M. Comparative stability analysis of synchronous reference frame current controllers operated at high fundamental frequency. *IEEE Trans. Transp. Electrif.* **2022**, *9*, 2115–2128. [CrossRef]
20. Fu, X.; Gu, S.; Xiong, J. Review of decoupling control methods for the DC and AC axes of permanent magnet synchronous motors. *Proc. CSEE* **2024**, *44*, 314–332.
21. Lin, K.; Lin, F.; Yang, Z. Research on decoupling control methods for permanent magnet synchronous motors. In Proceedings of the SPEED (2013), Shanghai, China, 6–8 April 2013; p. 7.
22. Harnefors, L.; Wang, X. Guest editorial: Special section on complex vector theory and its application in power electronic systems. *IEEE J. Emerg. Sel. Top. Power Electron.* **2020**, *8*, 1821–1823. [CrossRef]
23. Cui, K.; Wang, C.; Gou, L.; An, Z. Analysis and design of current regulators for PMSM drives based on DRGA. *IEEE Trans. Transp. Electrif.* **2020**, *6*, 659–667. [CrossRef]
24. Cloud, C.; Li, G.; Maslen, E.; Barrett, L.; Foiles, W. Practical applications of singular value decomposition in rotor dynamics. *Aust. J. Mech. Eng.* **2005**, *2*, 21–32. [CrossRef]
25. Liu, P.; Wang, Z.; Ding, L.; Xu, Y.; Li, Y.; Wang, B.; Cheng, M. Discrete-time complex-vector model based closed-loop current controller for CSC-fed PMAC machine systems with low carrier ratios. *IEEE Trans. Power Electron.* **2022**, *38*, 762–775. [CrossRef]
26. Li, Q.; Wang, D.; Lin, J.; Jian, F.; Wang, Z.; Ma, C. Improving dynamic accuracy of the electric motor emulator at high speed via MIMO design method. *IEEE Trans. Power Electron.* **2022**, *37*, 14395–14407. [CrossRef]

27. Yang, C.; Song, B.; Xie, Y.; Tang, X. Online parallel estimation of mechanical parameters for PMSM drives via a network of interconnected extended sliding-mode observers. *IEEE Trans. Power Electron.* **2021**, *36*, 11818–11834. [CrossRef]
28. Chang, H.; Wang, Z.; Yang, J.; Li, S.; Lu, S. Synchronous estimation scheme of PMSM mechanical parameters: A decoupled extended sliding-mode observer. *IEEE Trans. Power Electron.* **2025**, *40*, 10877–10888. [CrossRef]
29. Deshmukh, A.V.; Erturk, F.; Jena, S.; Akin, B. A robust inductance estimation method at standstill considering magnetic saturation. *IEEE Trans. Transp. Electrif.* **2024**, *11*, 6988–7001. [CrossRef]
30. Chinchul, C.; Wootaik, L. Analysis and compensation of time delay effects in hardware-in-the-loop simulation for automotive PMSM drive system. *IEEE Trans. Ind. Electron.* **2012**, *59*, 3403–3410. [CrossRef]
31. Bon-Ho, B.; Sul, S.-K. A compensation method for time delay of full-digital synchronous frame current regulator of PWM AC drives. *IEEE Trans. Ind. Appl.* **2003**, *39*, 802–810. [CrossRef]

**Disclaimer/Publisher's Note:** The statements, opinions and data contained in all publications are solely those of the individual author(s) and contributor(s) and not of MDPI and/or the editor(s). MDPI and/or the editor(s) disclaim responsibility for any injury to people or property resulting from any ideas, methods, instructions or products referred to in the content.